nature physics

Article

https://doi.org/10.1038/s41567-025-02799-8

The strongly driven Fermi polaron

Received: 22 January 2024

Accepted: 21 January 2025

Published online: 7 April 2025

Check for updates

Franklin J. Vivanco[1,6], Alexander Schuckert[2,6] ✉, Songtao Huang[1,6] ✉, Grant L. Schumacher[1], Gabriel G. T. Assumpção[1], Yunpeng Ji[1], Jianyi Chen[1], Michael Knap[3,4] & Nir Navon[1,5]

Quasiparticles are emergent excitations of matter that underlie much of our understanding of quantum many-body systems. Therefore, the prospect of controlling their properties has both fundamental and practical implications. However, in solid-state materials, it is often challenging to understand how quasiparticles are modified by external fields due to their complex interplay with other collective excitations. Here we demonstrate the manipulation of Fermi polarons—quasiparticles formed by impurities interacting with a Fermi gas—in a homogeneous atomic gas using fast radio-frequency control. Exploiting two internal states of the impurity species, we develop a steady-state spectroscopy, from which we extract the energy of the driven polaron. By varying the drive Rabi frequency, we measure the decay rate and the quasiparticle residue of the polaron in the weak-drive limit. At large Rabi frequencies, we observe signs that the drive causes a hybridization of the driven polaron with an incoherent background, leading to the breakdown of a description in terms of textbook quasiparticles. Our experiment establishes the driven Fermi polaron as a promising platform for studying controllable quasiparticles in strongly driven quantum matter and calls for a controlled theoretical framework to describe the dynamics of this strongly interacting quantum system.

The low-energy physics of quantum many-body systems can often be understood in terms of quasiparticle excitations. This description has been successful in explaining the thermodynamic and near-equilibrium transport properties of a wide range of materials[1]. Methods to modify, and even controllably destroy, these quasiparticles have long been sought after[2–4]. Such tuning capability could allow modifying the thermodynamics of a system, and potentially offer a route towards realizing strongly correlated systems without well-defined quasiparticles[5,6].

Fermi polarons—impurities that interact with a non-interacting Fermi gas—have attracted considerable interest because they constitute one of the simplest quantum many-body settings for studying both in-equilibrium and out-of-equilibrium properties in correlated systems[7–13]. Both attractive and repulsive Fermi polarons have been experimentally realized with ultracold atoms[9,10,14–19] and with semiconductor heterostructures[20]. Furthermore, Rabi oscillations of impurities with internal states that interact differently with the bath have been used to probe the properties of these polarons, though the interpretation of these experiments remains challenging[10,17,21–24]. Harnessing the non-equilibrium dynamics of driven Fermi polarons to manipulate their quasiparticle properties has, thus, remained a major challenge to both experiment and theory.

Here we investigate Fermi impurities embedded in a homogeneous atomic Fermi gas and driven with an external radio-frequency (rf) field as a platform for realizing quasiparticles with tunable properties (Fig. 1a). The impurities have two internal states: one of them essentially does not interact with the Fermi gas, whereas the other interacts

[1]Department of Physics, Yale University, New Haven, CT, USA. [2]Joint Quantum Institute and Joint Center for Quantum Information and Computer Science, University of Maryland and NIST, College Park, MD, USA. [3]Technical University of Munich, TUM School of Natural Sciences, Physics Department, Garching, Germany. [4]Munich Center for Quantum Science and Technology (MCQST), München, Germany. [5]Yale Quantum Institute, Yale University, New Haven, CT, USA. [6]These authors contributed equally: Franklin J. Vivanco, Alexander Schuckert, Songtao Huang. ✉e-mail: aschu@umd.edu; songtao.huang@yale.edu

https://doi.org/10.1038/s41567-025-02799-8

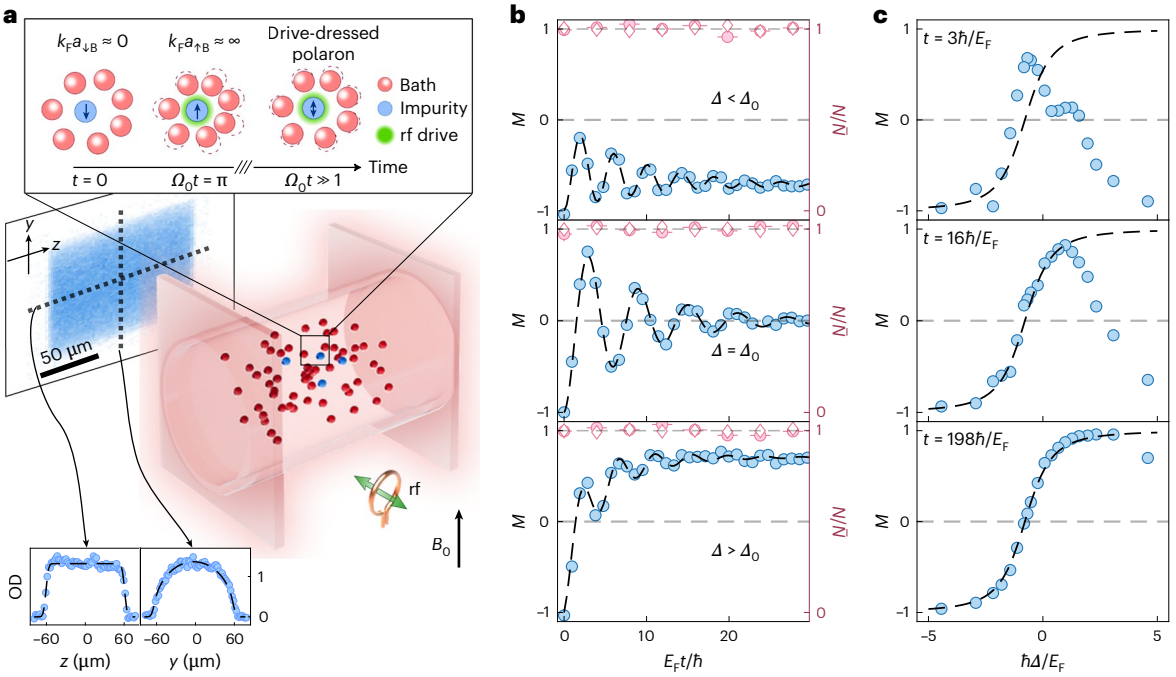

Fig. 1 | The strongly driven Fermi impurity. a, A uniform Fermi gas of ^{6}Li atoms is trapped in a cylindrical optical box. The red (blue) dots inside the box are bath (impurity) atoms. The image is a typical in situ optical density (OD) image of the impurity species (averaged over 14 realizations). The bottom insets show the central cuts of the OD image. The black dashed lines are fits to the density profiles. The top inset shows a cartoon of a typical Rabi oscillation experiment and subsequent dressing of the Fermi impurity by both its interactions with the bath and its coupling to the rf field, that is, the drive-dressed polaron. The impurity is initialized in state $|\downarrow\rangle$, which interacts weakly with $|B\rangle$. After a half-cycle, it is predominantly in $|\uparrow\rangle$, interacting strongly with $|B\rangle$. At long times, it reaches a steady state that is a mixture of states $|\uparrow\rangle$ and $|\downarrow\rangle$ (see the main text). **b**, Rabi oscillations of the magnetization M for three detunings Δ from the bare transition between $|\downarrow\rangle$ and $|\uparrow\rangle$ (full blue circles, left vertical axis), $\Delta/\Delta_0 = -0.3, 1, 2.4$ (from top to bottom); $\hbar/E_F \approx 25$ μs. The pink circles (diamonds) are the total impurity (bath) atom numbers $N = N_\uparrow + N_\downarrow$ ($N = N_B$), normalized by the atom number averaged over the whole time series $\bar{N}$ (right vertical axis). The vertical error bars are the standard error of the mean (s.e.m.), which is smaller than the marker size; the horizontal error bars correspond to the standard deviation of $E_F t/\hbar$ in each time bin. **c**, Magnetization as a function of detuning with pulse time t increasing from top to bottom. In **b** and **c**, the Rabi frequency is $\Omega_0/(2\pi) \approx 8$ kHz, and the black dashed lines are guides to the eye.

unitarily with it. We drive the impurity by coupling the two internal states with the rf field and probe the impurities dressed by both their interactions with the bath and their coupling to the rf field; we measure their quasiparticle properties—energy, decay rate and residue—as a function of the drive strength.

Our experiment begins with a spatially uniform quantum gas of ^{6}Li atoms confined in an optical box[25,26] (Fig. 1a). The gas is in a highly imbalanced mixture of the internal states $|\downarrow\rangle$ and $|B\rangle$, where $|\downarrow\rangle$ is one of the two internal states of the impurity and $|B\rangle$ is the bath state that forms the Fermi gas. The bath has a Fermi energy $E_F/\hbar \approx 2\pi \times 6$ kHz and a temperature $T = 0.25(2)T_F$, where T_F is the Fermi temperature of the bath and $\hbar$ is the reduced Planck constant (Methods and Supplementary Sections II and III). The magnetic field is set to the Feshbach resonance B_0 of the $|\uparrow\rangle$–$|B\rangle$ mixture, whereas $|\downarrow\rangle$ and $|B\rangle$ are weakly interacting; that is, $1/k_F a_{\uparrow B} = 0$ and $k_F a_{\downarrow B} \approx 0.16$; $|\uparrow\rangle$ is the second internal state of the impurity, k_F is the Fermi wavevector of the bath and $a_{\uparrow B}$ ($a_{\downarrow B}$) is the s-wave scattering length between states $|\uparrow\rangle$ ($|\downarrow\rangle$) and $|B\rangle$. An in situ optical density image of the impurity species $|\downarrow\rangle$ is shown in Fig. 1a, along with two central cuts.

After initialization, an rf field of Rabi frequency Ω_0 and detuning Δ (relative to the bare $|\downarrow\rangle$–$|\uparrow\rangle$ transition) is turned on for a duration t. We then measure the magnetization of the impurities $M \equiv (N_\uparrow - N_\downarrow)/(N_\uparrow + N_\downarrow)$ as a function of t, where $N_\uparrow$ ($N_\downarrow$) is the population of the impurities in state $|\uparrow\rangle$ ($|\downarrow\rangle$). In Fig. 1b, we show typical measurements of the dynamics of the magnetization for different detunings. For all the detunings, we observe damped Rabi oscillations, which reach a detuning-dependent steady-state value at long times. The dependence of the magnetization on the detuning is visualized in Fig. 1c, where we show the magnetization as a function of detuning for various evolution times. At short times, we see a sharp peak with a broad shoulder reminiscent of the linear-response spectrum at unitarity[10,12,17] (our measurement would be equivalent to the linear-response injection spectroscopy if performed in the regime of weak drive ($\hbar\Omega_0/E_F \ll 1$) and short times (for which $M \approx -1$)). However, at longer times, we find a strong deviation from linear-response-type behaviour; in fact, M converges to a monotonously increasing function of Δ in the steady state (Fig. 1c, black dashed lines). The steady-state magnetization spectrum $M(\Delta)$ vanishes at detuning Δ_0, the zero crossing.

We now study how $M(\Delta)$ varies with the drive strength $\hbar\Omega_0/E_F$. In Fig. 2a, we show the steady-state spectra for $\hbar\Omega_0/E_F = 1.1$ and 9.2. Although the zero crossing and the typical width of the spectra depend on $\hbar\Omega_0/E_F$, Fig. 2a (inset) shows that the spectra collapse onto a universal curve when the detuning is rescaled to $(\Delta - \Delta_0)/\Omega_0$, where Δ_0 depends on Ω_0.

A first description of this behaviour is provided by the ground state of an effective spin 1/2 coupled to a field of Rabi frequency $\tilde{\Omega}$ and detuning $\tilde{\Delta}$ from its resonance (Supplementary Section I):

$$M_0 = \frac{\tilde{\Delta}}{\sqrt{\tilde{\Omega}^2 + \tilde{\Delta}^2}}. \quad (1)$$

Our measured magnetization is indeed well described by this model when setting $\tilde{\Delta} = \Delta - \Delta_0$ and $\tilde{\Omega} = \Omega_0$ (Fig. 2a, black dashed line). This model captures the rescaling of the spectrum, with $M_0 = f(\tilde{\Delta}/\Omega_0)$ and $f(x) = x/\sqrt{1+x^2}$.

This universality suggests that our protocol realizes a novel steady-state spectroscopy, that is, the response of the many-body

https://doi.org/10.1038/s41567-025-02799-8

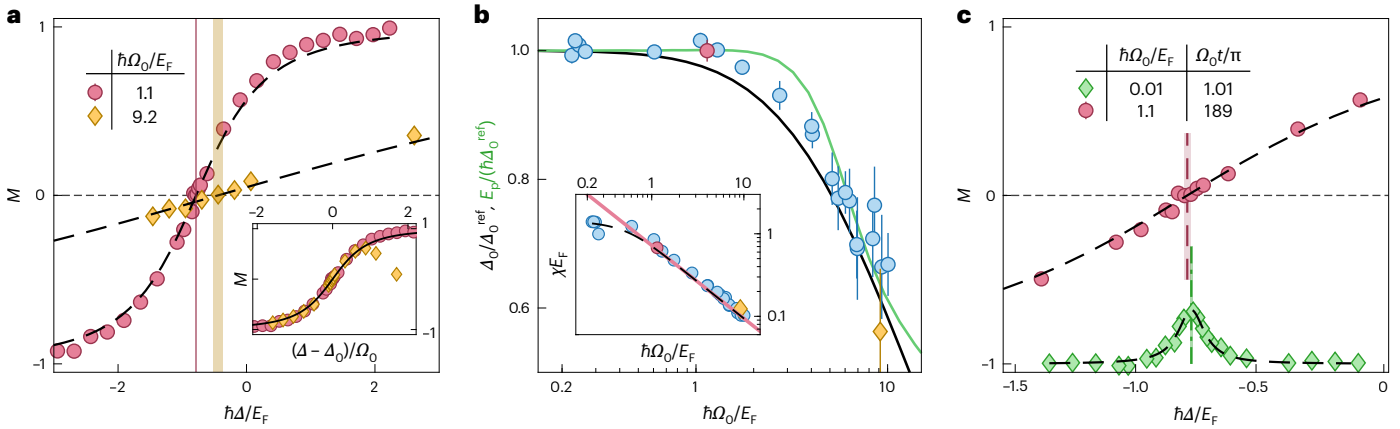

Fig. 2 | Many-body steady-state spectroscopy. a, Steady-state spectra measured for two Rabi frequencies. The black dashed lines are fits to equation (1). The red and orange vertical bands mark the zero crossing Δ_0 including the fitting uncertainty. The inset shows the scaling collapse of the steady-state spectra. The black solid line corresponds to equation (1). **b**, Normalized zero crossing versus drive strength. The blue, red and orange points are the experimental data for Δ_0 (Methods); the red and orange points correspond to the spectra shown in **a**. The error bars are the uncertainties of the fits. The black (green) solid line is the theoretical prediction for Δ_0 (drive-dependent polaron energy E_p), including the effect of finite temperature and corrections due to the non-zero $k_F a_{\uparrow B}$ (the main text discusses the difference between E_p and Δ_0). The normalization is chosen to be the weak-drive limit $\hbar\Delta_0^{ref}/E_F = -0.78$ (−0.73) for the experimental data (theory). The data normalized to E_F are shown in Supplementary Fig. 8. The inset shows the susceptibility χ versus drive strength. The red solid line is the susceptibility of the ground state (equation (1)). The black dashed line is a fit to the $T > 0$ generalization of the model in equation (1) (see the main text). **c**, Comparison of the linear-response injection spectroscopy (green diamonds) and steady-state spectroscopy (red circles). The black dashed lines are a fit of the steady-state spectrum (a linear-response spectrum) to equation (1) (a Lorentzian function). The red dashed line (green dash–dotted line) is the fitted zero crossing (linear-response peak position); the bands are the corresponding fitting uncertainties. The error bars in **a** and **c** are the s.e.m. values of three measurements and are smaller than the marker size.

system is captured by a small number of (drive-dependent) parameters (in this case, Δ_0 and the response's typical width). Interestingly, Δ_0 shifts closer to zero with increasing drive strength (Fig. 2a, vertical colour bands). To quantify this effect, we show the extracted Δ_0 value over nearly two orders of magnitude of the drive strength in Fig. 2b. We also extract the typical width of the spectrum (Fig. 2b, inset), which we characterize by the on-resonance susceptibility $\chi \equiv (\partial M/\partial\Delta)|_{\Delta=\Delta_0}$. The behaviour of $\chi(\Omega_0)$ is well explained with the finite-temperature generalization of the model equation (1) (Supplementary Section I): for such a system, the $T > 0$ magnetization is given by $M = M_0 \tanh\left(\sqrt{(\hbar\Omega_0)^2 + (\hbar\tilde{\Delta})^2}/(2k_B T_{spin})\right)$. A fit of the measured χ to this model yields a spin (that is, the internal-state) temperature for the impurity of $T_{spin} = 0.24(1)T_F$ (Fig. 2b (inset), black dashed line). Because the finite-temperature correction becomes negligible when $\hbar\Omega_0 \gtrsim 2k_B T_{spin}$, the impurity is effectively in its internal ground state for $\hbar\Omega_0 \gtrsim E_F$ (Fig. 2b (inset), black dashed line and red solid line).

The fact that the spin temperature T_{spin} matches the bath temperature T indicates that the internal degrees of freedom of the driven polaron have thermalized with the fermionic bath. Two additional observations support the fact that our system consisting of the impurities plus the bath obeys closed-system dynamics. First, the coherence time of the Rabi oscillations in the absence of the bath exceeds—by about two orders of magnitude—the typical duration of our experiments in the presence of the bath. Thus, the decay is not due to dephasing caused by, for instance, magnetic-field noise or inhomogeneity (Supplementary Section IV). Second, the impurity and bath atom numbers are constant during the dynamics (Fig. 1b, pink symbols).

A non-trivial shift in the zero crossing, $\Delta_0 \neq 0$, is a prime indication of interactions between the impurity and the Fermi gas. To gain insight into Δ_0, we measure the rf linear-response injection spectrum, that is, the fraction of impurities transferred from $|\downarrow\rangle$ into $|\uparrow\rangle$ using a weak rf pulse ($\hbar\Omega_0 \ll E_F$). A typical measurement is shown in Fig. 2c (green diamonds). We find that Δ_0 matches the location of the peak E_p of the linear-response spectrum (that is, the energy of the attractive polaron[18]), even for a steady-state spectrum taken at a moderate rf power $\hbar\Omega_0 \approx E_F$ (Fig. 2c, red points). We thus conclude that the plateau at low $\hbar\Omega_0/E_F$ (Fig. 2b) matches the linear-response peak position. However, with increasing drive strength $\hbar\Omega_0/E_F \gtrsim 1$, the zero crossing smoothly departs from its low-Ω_0 plateau, towards zero.

We compare our measurements with the predictions of a diagrammatic theory based on the non-self-consistent T matrix (Methods and Supplementary Section I). We directly include the drive in the T matrix[23] to describe the drive-induced changes in the scattering properties of the impurities. We also include corrections due to the non-zero $a_{\uparrow B}$ (Methods). In Fig. 2b, the black line shows the theoretical prediction for $\Delta_0(\Omega_0)$, calculated from the spectral functions (Methods and Supplementary Section I); the theoretical Δ_0 is normalized to its weak-drive limit $\Delta_0^{ref} \equiv \Delta_0(\Omega_0 \to 0)$. We find a behaviour that qualitatively reproduces the experimental data. Furthermore, we find that the polaron energy, defined as the solution of $E_p = \mathrm{Re}\Sigma(E_p)$ (where Σ is the zero-momentum self-energy of the impurity evaluated at the Rabi frequency Ω_0 and detuning Δ_0), matches the theoretical $\hbar\Delta_0$ in the limit $\hbar\Omega_0/E_F \to 0$ (ref. 27), reproducing the experimental finding shown in Fig. 2c. Interestingly, E_p is in remarkable agreement with the experimental data, when normalized to the weak-drive limit Δ_0^{ref} (Fig. 2b, green solid line). This observation suggests that Δ_0 may be the dressed polaron energy at all drive strengths, and motivates the development of more refined methods to calculate Δ_0.

We now study the pre-steady-state dynamics, focusing on the resonant case $\Delta = \Delta_0$. The magnetization undergoes damped oscillations towards $M = 0$ (Fig. 1b, middle). We find that the data are well fitted by $M(t) = -\cos(\Omega_R t)\exp(-\Gamma t/2)$, from which we extract a renormalized Rabi frequency Ω_R and a decay rate Γ (Methods).

These quantities have been connected to the equilibrium properties of the polaron[10,17,22]. By assuming that the bath is not perturbed by the impurities (and that $\hbar\Omega_0 \ll E_F$, such that the Rabi oscillations are underdamped), the dynamics of the Rabi oscillations at early times can be approximately captured by an equilibrium correlation function that is given at low temperature by the impurity's zero-momentum spectral function in the presence of the drive (Supplementary Section I). This approach leads to the following expressions for the zero-momentum

https://doi.org/10.1038/s41567-025-02799-8

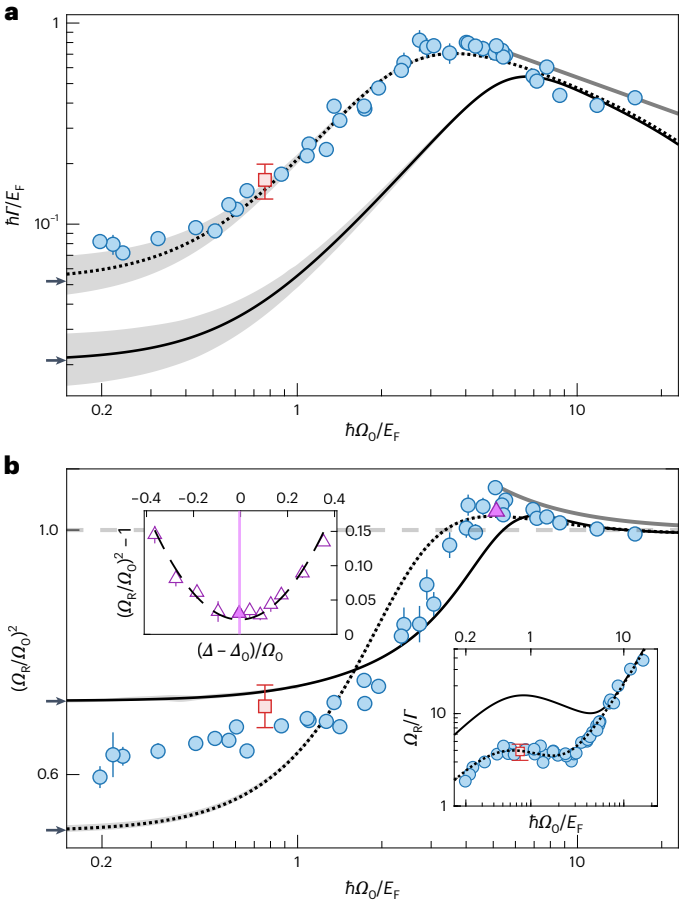

Fig. 3 | Dynamical properties of the driven Fermi polaron. a,**b**, Decay rate Γ (**a**) and renormalized Rabi frequency Ω_R (**b**) extracted from the Rabi oscillations on resonance $\Delta = \Delta_0$ (Fig. 1b (middle) shows an example). The red squares are the measurements from ref. 17 and the purple triangle in **b** refers to the measurement in the inset. The black solid (dotted) lines are the theoretical predictions using the in-medium (two-body) T matrix, with error bands evaluated from the experimental uncertainty on the temperature. The arrows indicate the theoretical predictions at $\Omega_0 = 0$. The grey solid line is the analytical result in the limit of $\hbar\Omega_0/E_F \gg 1$ (assuming $k_F a_{\uparrow B} = 0$ and $T = 0$). The error bars are the uncertainties of the fits. The top inset shows $(\Omega_R/\Omega_0)^2 - 1$ as a function of the detuning relative to the zero crossing. The solid point refers to the measurement in the main panel. The dashed line is a quadratic fit. The vertical solid line marks the centre of the fit, $\Delta/\Delta_0 = 1.03(5)$. Except for this inset, Ω_R is measured at $\Delta = \Delta_0$. The bottom inset shows Ω_R/Γ versus $\hbar\Omega_0/E_F$ extracted from the data in **a** and **b**.

quasiparticle decay rate Γ and the renormalized Rabi frequency Ω_R in terms of the impurity self-energy Σ (refs. 22,23): $\hbar\Gamma = -2Z\,\mathrm{Im}\Sigma(E = E_p)$ and $\Omega_R = \sqrt{Z}\Omega_0$ (ref. 10), where $Z = 1/\left(1 - \frac{\partial(\mathrm{Re}\Sigma)}{\partial E}|_{E=E_p}\right)$ is the quasiparticle residue, which is the overlap between the Fermi polaron wavefunction and the non-interacting impurity wavefunction.

In Fig. 3a, we show Γ as a function of the drive strength, along with the T-matrix predictions. At our weakest drives, the decay rate appears to slowly level off. Note that a previous measurement at a given Ω_0 is in good agreement with our data (Fig. 3, red square[17]). For stronger drives, that is, $\hbar\Omega_0 \gtrsim E_F$, Γ shows an unexpected non-monotonic behaviour. First, it increases by over an order of magnitude between our lowest Ω_0 and a maximum located at around $\hbar\Omega_0/E_F \approx 3$; it then decreases as a power law of the drive strength.

We use the T-matrix approach to calculate Γ (Fig. 3a, black solid line). It is in qualitative agreement with the data but is quantitatively imprecise for all but the largest drives. The power law at large drive strengths originates from the properties of the two-body scattering: scattered particles have an energy $\propto\hbar\Omega_0$ and the T matrix is dominated by the two-body contribution, so that it is proportional to the inverse square root of Ω_0 (ref. 28). Our data are in good agreement with the corresponding analytical prediction $\hbar\Gamma/E_F \approx 16/\left(3\pi\sqrt{\hbar\Omega_0/E_F}\right)$ (Fig. 3a, grey line). Motivated by this observation, we introduce a two-body T-matrix approximation that neglects in-medium scattering effects but still takes into account the presence of the Fermi sea in the self-energy (Fig. 3a, black dotted line). Surprisingly, this approximation captures the data remarkably well for all drive strengths.

The linear-response spectrum provides another measure for the quasiparticle decay rate. From our injection spectroscopy measurements (Fig. 2c, green points), we extract a width $\Gamma_{\mathrm{lin}} = 0.13(2)E_F/\hbar$, which is close to the width measured by ejection spectroscopy[18]. This width is a little larger than our weakest-drive $\Gamma = 0.072(5)E_F/\hbar$ (Fig. 3a). It is possible that a finite impurity concentration could have a different effect on the Rabi dynamics and the linear-response spectroscopy[23]. Their respective relationship to the linear-response properties in the impurity limit is not straightforward and remains to be clarified[10,22].

The normalized (dynamical) Rabi frequency Ω_R/Ω_0 extracted from the damped oscillations also depends on the bare Rabi frequency Ω_0. In Fig. 3b, we show Ω_R/Ω_0 versus $\hbar\Omega_0/E_F$. At $\hbar\Omega_0/E_F \approx 2$, Ω_R/Ω_0 abruptly increases, reaches a maximum exceeding the one at around $\hbar\Omega_0/E_F \approx 5$ and then decreases towards one. In the regime of strong drives, we find $\Omega_R > \Omega_0$. An explanation for this effect could have been that the minimum of Ω_R is not reached at the detuning $\Delta = \Delta_0$. However, we measure Ω_R as a function of the detuning (Fig. 3b, top inset) and find that Ω_R is consistently larger than Ω_0; its minimum is reached at $\Delta = 1.03(5)\Delta_0$.

To settle the range of $\hbar\Omega_0/E_F$ over which our Rabi oscillation spectroscopy is valid, we show the quality factor of the Rabi oscillations Ω_R/Γ in Fig. 3b (bottom inset). At weak drives, Ω_R/Γ roughly plateaus; at even weaker drives ($\hbar\Omega_0 \lesssim 0.4E_F$), the ratio decreases further and oscillations ultimately become overdamped (Supplementary Section V shows a set of measurements across the critical damping threshold).

The observation that Ω_R can exceed Ω_0 is at odds with the expectation that $(\Omega_R/\Omega_0)^2$ is the quasiparticle residue. Indeed, the residue Z, defined as the area under the quasiparticle peak in the spectral function, must always be ≤ 1. We can formally define a pseudo-residue $\tilde{Z} \equiv 1/\left(1 - \frac{\partial(\mathrm{Re}\Sigma)}{\partial E}|_{E=E_p}\right)$, which coincides with Z for textbook quasiparticles[29] (and is often used as a definition for the residue[30]). We find that both two-body and in-medium T-matrix approximations predict that $\tilde{Z}$ follows a similar behaviour to $(\Omega_R/\Omega_0)^2$ (Fig. 3b, dotted and solid black lines, respectively), suggesting the intriguing generalization $(\Omega_R/\Omega_0)^2 \approx \tilde{Z}$. In particular, we analytically calculate $\tilde{Z} \approx 1 + 16/(6\pi(\hbar\Omega_0/E_F)^{3/2}) > 1$ in the limit $\hbar\Omega_0/E_F \gg 1$ (Supplementary Section I). This prediction (Fig. 3b, grey line) is in very good agreement with our measurements. The fact that $\tilde{Z} > 1$ indicates that the standard description of a (Lorentzian-shaped) quasiparticle breaks down. This is another interesting illustration of a textbook quasiparticle breakdown that is not signalled by the usual criterion $\tilde{Z} \to 0$ (as in the case of immobile Fermi impurity[31,32]); see, for example, a recent condensed-matter experiment in which a quasiparticle disappearance, accompanied by an increase in Z, was caused by a widening of the quasiparticle into an incoherent background[30].

This finding motivates us to examine the quasiparticle quality factor Q, defined as the ratio of the quasiparticle energy and its decay rate. Using the zero crossing as a proxy for the drive-dressed polaron energy, we define $Q \equiv \Delta_0/\Gamma$. In Q versus $\hbar\Omega_0/E_F$ (Fig. 4a), we find that $Q \gg 1$ for low Ω_0, indicating a well-defined polaron. However, the quality factor decreases by over an order of magnitude to a minimum of ≈ 0.9 at $\hbar\Omega_0/E_F \approx 4$, indicating that the polaron is no longer well defined, specifically, it is close to the critical damping threshold $Q = 1/2$.

The fact that $Q \approx 1$ in conjunction with $(\Omega_R/\Omega_0)^2 > 1$ at $\hbar\Omega_0/E_F \approx 4$ further substantiates the failure of the textbook quasiparticle picture in that regime. We have seen earlier that the pseudo-residue $\tilde{Z}$ defined

https://doi.org/10.1038/s41567-025-02799-8

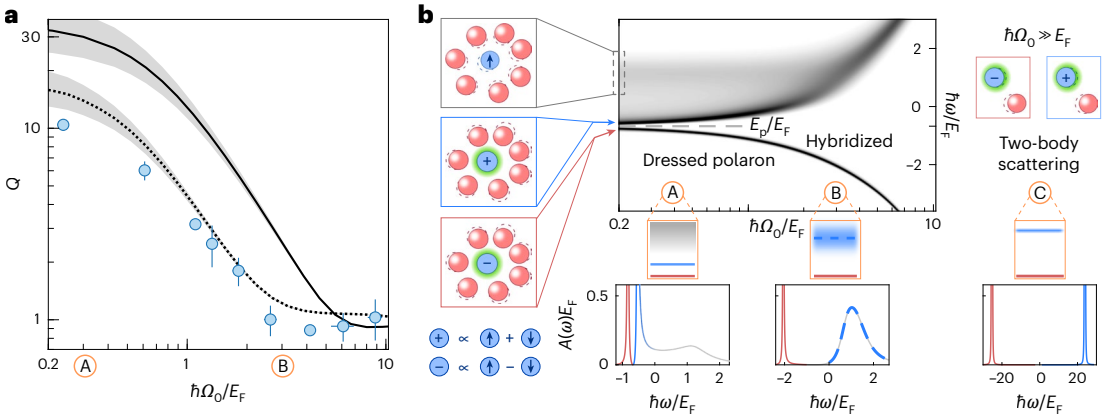

Fig. 4 | Quasiparticle quality factor of the driven polaron. a, The quality factor $Q \equiv \Delta_0/\Gamma$ of the driven polaron measured in the bare-state basis $\{|\uparrow\rangle, |\downarrow\rangle\}$ is extracted from the data in Fig. 3a and Supplementary Fig. 8 (by binning). The solid (dotted) line is the theoretical prediction using the in-medium (two-body) T matrix, with the error bands indicating the experimental uncertainty in the temperature. The horizontal error bars correspond to the standard deviation of the drive strength in each bin, and the vertical error bars are calculated from the uncertainties of the fits within each bin. The regimes labelled A and B correspond to the weak ($\hbar\Omega_0/E_F \ll 1$) and strong ($\hbar\Omega_0/E_F \gtrsim 1$) regimes, respectively. **b**, Energy diagram of the driven polaron calculated using the in-medium T matrix (Supplementary Section I). Left: a cartoon illustration of the effective states in regime A. An incoherent continuum of states, the unitary-limit remnant of the repulsive polaron, is shown in the grey box; the two drive-dressed attractive polaron states are shown in the blue and red boxes, where $|\pm\rangle = |\uparrow\rangle \pm |\downarrow\rangle)/\sqrt{2}$. Middle: theoretical energy diagram. At weak drive strength (A), the two drive-dressed states are unaffected by the continuum, their energy is $\approx E_p$ and their splitting is $\hbar\Omega_0$. At intermediate drive strength (B), one of the dressed polarons $|+\rangle$ is pushed up and merges with the continuum. Right: in the ultrastrong regime $\hbar\Omega_0/E_F \gg 1$ (labelled C; not accessed in this work), two-body scattering dominates and results in two well-defined states (right). Bottom: spectral functions of the driven polaron calculated at $\hbar\Omega_0/E_F = 0.4, 3, 50$ (from left to right; Supplementary Fig. 5), where the colour scheme follows the states in the cartoons of the left panel.

through the Taylor expansion of the self-energy around the polaron energy E_p yields non-physical values for the quasiparticle residue. We indeed find that within the T-matrix calculations, $\tilde{Z}$ depends on the energy at which it is evaluated, even within the spectral width Γ; this goes beyond the usual quasiparticle paradigm (Supplementary Section I). Nevertheless, it is intriguing that even though $\tilde{Z}$ (>1) is no longer the quasiparticle residue in the strong-drive regime, its formal expression is in good agreement with the measured $(\Omega_R/\Omega_0)^2$.

Putting all this together, we can now interpret the different regimes of the driven polaron. As shown in the energy diagram (Fig. 4b; built from the theoretical spectral function), there are three distinct regimes. In the first weak-drive regime $\hbar\Omega_0/E_F \ll 1$ (labelled A), there are three spectral features. The attractive polaron is split into two rf-dressed states $|\pm\rangle = (|\uparrow\rangle \pm |\downarrow\rangle)/\sqrt{2}$ (red and blue boxes), whose energy separation is roughly $\propto \hbar\Omega_0$. The third feature is the remnant of the unstable repulsive polaron, seen as the broad continuum at high energies; it is basically unaffected by the rf. In the strong-drive regime $1 \lesssim \hbar\Omega_0/E_F \lesssim 10$ (labelled B), the dressed state $|+\rangle$ is pushed into the continuum and hybridization leads to the disintegration of the quasiparticle for $\hbar\Omega_0/E_F \approx 3$. For ultrastrong drives $\hbar\Omega_0/E_F \gtrsim 10$ (labelled C), which we do not reach experimentally, many-body effects (dominated by two-body scattering) are a perturbation to the large rf splitting and the driven impurity essentially behaves as a dressed two-level system. In the experiment, we are probing the transient (Rabi) dynamics of the system towards thermalization after a rapid quench into a superposition of those dressed states; the hybridization manifests itself as the non-monotonic evolution of Γ and Ω_R around $\hbar\Omega_0/E_F \approx 3$ (Supplementary Section I). This interpretation, although based on the standard but unsettled connection between the Rabi oscillations and the equilibrium spectral function, is supported by the good agreement between our experimental observation and our calculations.

In conclusion, we have shown that the driven impurity in a Fermi gas is a powerful platform for studying non-equilibrium quantum dynamics. In the future, our many-body steady-state spectroscopy could be used to study many-body systems without well-defined quasiparticles, such as the spin-balanced unitary Fermi gas in the normal phase[33], or the heavy impurity system[34,35]. It would also be interesting to study how polaron–polaron interactions could be modified by the drive, as well as observe the dressed-state polarons with a secondary (probing) field. Furthermore, in the $1/k_F a_{\uparrow B} > 0$ regime, one could observe richer steady-state magnetization spectra for pre-thermal states containing both stable attractive and repulsive polarons[34]. Theoretically, it is imperative to establish a systematic theoretical framework to elucidate the connection between the impurity's equilibrium spectral properties and the Rabi oscillations, since the reasonable agreement of the measurements of both Ω_R and Γ with our (state-of-the-art yet uncontrolled) T-matrix calculations is rather surprising. This could be done, for example, by using the Keldysh approach[24].

Online content

Any methods, additional references, Nature Portfolio reporting summaries, source data, extended data, supplementary information, acknowledgements, peer review information; details of author contributions and competing interests; and statements of data and code availability are available at https://doi.org/10.1038/s41567-025-02799-8.

References

1. Landau, L. D. The theory of a Fermi liquid. *Zh. Eksp. Teor. Fiz.* **30**, 1058 (1956).
2. Basov, D., Averitt, R. & Hsieh, D. Towards properties on demand in quantum materials. *Nat. Mater.* **16**, 1077–1088 (2017).
3. de la Torre, A. et al. Colloquium: nonthermal pathways to ultrafast control in quantum materials. *Rev. Mod. Phys.* **93**, 041002 (2021).
4. Bloch, J., Cavalleri, A., Galitski, V., Hafezi, M. & Rubio, A. Strongly correlated electron–photon systems. *Nature* **606**, 41–48 (2022).
5. Coleman, P., Pépin, C., Si, Q. & Ramazashvili, R. How do Fermi liquids get heavy and die?. *J. Phys. Condens. Matter* **13**, R723 (2001).
6. Hartnoll, S. A., Lucas, A. & Sachdev, S. *Holographic Quantum Matter* (MIT Press, 2018).
7. Radzihovsky, L. & Sheehy, D. E. Imbalanced Feshbach-resonant Fermi gases. *Rep. Progr. Phys.* **73**, 076501 (2010).
8. Chevy, F. & Mora, C. Ultra-cold polarized Fermi gases. *Rep. Progr. Phys.* **73**, 112401 (2010).

9. Schirotzek, A., Wu, C.-H., Sommer, A. & Zwierlein, M. W. Observation of Fermi polarons in a tunable Fermi liquid of ultracold atoms. *Phys. Rev. Lett.* **102**, 230402 (2009).
10. Kohstall, C. et al. Metastability and coherence of repulsive polarons in a strongly interacting Fermi mixture. *Nature* **485**, 615–618 (2012).
11. Massignan, P., Zaccanti, M. & Bruun, G. M. Polarons, dressed molecules and itinerant ferromagnetism in ultracold Fermi gases. *Rep. Progr. Phys.* **77**, 034401 (2014).
12. Cetina, M. et al. Ultrafast many-body interferometry of impurities coupled to a Fermi sea. *Science* **354**, 96–99 (2016).
13. Scazza, F., Zaccanti, M., Massignan, P., Parish, M. M. & Levinsen, J. Repulsive Fermi and Bose polarons in quantum gases. *Atoms* **10**, 55 (2022).
14. Nascimbène, S. et al. Collective oscillations of an imbalanced Fermi gas: axial compression modes and polaron effective mass. *Phys. Rev. Lett.* **103**, 170402 (2009).
15. Koschorreck, M. et al. Attractive and repulsive Fermi polarons in two dimensions. *Nature* **485**, 619–622 (2012).
16. Zhang, Y., Ong, W., Arakelyan, I. & Thomas, J. E. Polaron-to-polaron transitions in the radio-frequency spectrum of a quasi-two-dimensional Fermi gas. *Phys. Rev. Lett.* **108**, 235302 (2012).
17. Scazza, F. et al. Repulsive Fermi polarons in a resonant mixture of ultracold ^{6}Li atoms. *Phys. Rev. Lett.* **118**, 083602 (2017).
18. Yan, Z. et al. Boiling a unitary Fermi liquid. *Phys. Rev. Lett.* **122**, 093401 (2019).
19. Darkwah Oppong, N. et al. Observation of coherent multiorbital polarons in a two-dimensional Fermi gas. *Phys. Rev. Lett.* **122**, 193604 (2019).
20. Sidler, M. et al. Fermi polaron-polaritons in charge-tunable atomically thin semiconductors. *Nat. Phys.* **13**, 255–261 (2017).
21. Parish, M. M. & Levinsen, J. Quantum dynamics of impurities coupled to a Fermi sea. *Phys. Rev. B* **94**, 184303 (2016).
22. Adlong, H. S. et al. Quasiparticle lifetime of the repulsive Fermi polaron. *Phys. Rev. Lett.* **125**, 133401 (2020).
23. Hu, H. & Liu, X.-J. Fermi spin polaron and dissipative Fermi-polaron Rabi dynamics. *Phys. Rev. A* **108**, 063312 (2023).
24. Wasak, T., Sighinolfi, M., Lang, J., Piazza, F. & Recati, A. Decoherence and momentum relaxation in Fermi-polaron Rabi dynamics: a kinetic equation approach. *Phys. Rev. Lett.* **132**, 183001 (2024).
25. Mukherjee, B. et al. Homogeneous atomic Fermi gases. *Phys. Rev. Lett.* **118**, 123401 (2017).
26. Navon, N., Smith, R. P. & Hadzibabic, Z. Quantum gases in optical boxes. *Nat. Phys.* **17**, 1334–1341 (2021).
27. Mulkerin, B. C., Levinsen, J. & Parish, M. M. Rabi oscillations and magnetization of a mobile spin-1/2 impurity in a Fermi sea. *Phys. Rev. A* **109**, 023302 (2024).
28. Shkedrov, C. et al. Absence of heating in a uniform Fermi gas created by periodic driving. *Phys. Rev. X* **12**, 011041 (2022).
29. Negele, J. W. *Quantum Many-Particle Systems* (CRC Press, 2018).
30. Hunter, A. et al. Fate of quasiparticles at high temperature in the correlated metal Sr_2RuO_4. *Phys. Rev. Lett.* **131**, 236502 (2023).
31. Goold, J., Fogarty, T., Lo Gullo, N., Paternostro, M. & Busch, T. Orthogonality catastrophe as a consequence of qubit embedding in an ultracold Fermi gas. *Phys. Rev. A* **84**, 063632 (2011).
32. Knap, M. et al. Time-dependent impurity in ultracold fermions: orthogonality catastrophe and beyond. *Phys. Rev. X* **2**, 041020 (2012).
33. Mukherjee, B. et al. Spectral response and contact of the unitary Fermi gas. *Phys. Rev. Lett.* **122**, 203402 (2019).
34. Knap, M., Abanin, D. A. & Demler, E. Dissipative dynamics of a driven quantum spin coupled to a bath of ultracold fermions. *Phys. Rev. Lett.* **111**, 265302 (2013).
35. Adlong, H. S., Liu, W. E., Turner, L. D., Parish, M. M. & Levinsen, J. Signatures of the orthogonality catastrophe in a coherently driven impurity. *Phys. Rev. A* **104**, 043309 (2021).

Methods

Preparation of a highly imbalanced uniform Fermi gas

We prepare an incoherent mixture of the first and third lowest Zeeman sub-levels (denoted as $|\uparrow\rangle$ and $|\mathrm{B}\rangle$) of ^{6}Li atoms in a red-detuned optical dipole trap. The internal states of the impurity species are $|\uparrow\rangle \equiv |\frac{1}{2}, +\frac{1}{2}\rangle$ and $|\downarrow\rangle \equiv |\frac{1}{2}, -\frac{1}{2}\rangle$ and the bath internal state is $|\mathrm{B}\rangle \equiv |\frac{3}{2}, -\frac{3}{2}\rangle$, in the $|F, m_F\rangle$ basis at a low magnetic field (F and m_F are the total spin and its projection along the magnetic-field axis, respectively). We evaporatively cool this mixture at a magnetic field of $B \approx 284$ G, where the s-wave scattering length between $|\uparrow\rangle$ and $|\mathrm{B}\rangle$ is $a_{\uparrow\mathrm{B}} \approx -900 a_0$. The atoms in state $|\uparrow\rangle$ are then transferred into state $|\downarrow\rangle$ with a 5-ms Landau–Zener rf sweep. After a 100-ms hold, we adiabatically ramp the field to $B \approx 583$ G in 500 ms, where $a_{\downarrow\mathrm{B}} \approx 0$, and then load the atoms into a blue-detuned optical box trap, formed by the intersection of two beams (wavelength, 639 nm) shaped by digital micromirror devices. The radius and length of the cylindrical box are $R = 63(1)$ μm and $L = 121(1)$ μm, respectively. We adjust the concentration $x \equiv N_\downarrow/N_\mathrm{B}$ (where N_B is the bath atom number) to be typically 0.17(2), by optically blasting atoms in $|\downarrow\rangle$ with a 12-μs light pulse of controllable intensity (Supplementary Section III). Finally, we ramp the field to $B_0 \approx 690$ G and hold it for 400 ms for equilibration. Typically, we have $N_\mathrm{B} \approx 5 \times 10^5$ atoms in the bath state, and the bath temperature is $T = 0.25(2) T_\mathrm{F}$ (measured by time-of-flight expansion of the weakly interacting mixture $|\downarrow\rangle$–$|\mathrm{B}\rangle$). To estimate the uncertainty due to the interaction between the impurity and the bath, we ramp the field back to 583 G to measure the temperature, which is within the error bar of the one extracted at 690 G.

Extracting the renormalized Rabi frequency and decay rate

To extract Ω_R and Γ on resonance, we fit the time evolution of magnetization with $M(t) = -\cos(\Omega_\mathrm{R} t)\exp(-\Gamma t/2)$. The off-resonant Rabi oscillation (Fig. 1b) is fitted with a phenomenological model $M(t) = M_\infty(\tilde{\Delta}) - A\exp(-\Gamma t/2)\cos(\Omega_\mathrm{R} t) - (1 - A + M_\infty(\tilde{\Delta}))\exp(-\Gamma' t/2)$, where $M_\infty(\tilde{\Delta})$ is the asymptotic magnetization and Γ and Γ' are the decay rates.

Model Hamiltonian of the system

As the largest detuning used in the experiment ($\lesssim$100 kHz) is much smaller than the transition frequency between the $|\uparrow\rangle$ and $|\downarrow\rangle$ states ($\approx$ 76.0 MHz), we can use the rotating-wave approximation. Within this approximation, the energy is conserved in the frame rotating with the drive. The Hamiltonian in that frame is

$$H = \frac{\hbar\Omega_0}{2}\sum_{\mathbf{k}}\left(c^\dagger_{\mathbf{k}\downarrow}c_{\mathbf{k}\uparrow} + \mathrm{h.c.}\right) + \sum_{\mathbf{k}}(\epsilon_{\mathbf{k}} + \hbar\Delta)c^\dagger_{\mathbf{k}\downarrow}c_{\mathbf{k}\downarrow} + \sum_{\mathbf{k}}\epsilon_{\mathbf{k}}c^\dagger_{\mathbf{k}\uparrow}c_{\mathbf{k}\uparrow} + \sum_{\mathbf{k}}(\epsilon_{\mathbf{k}} - \mu)d^\dagger_{\mathbf{k}}d_{\mathbf{k}} + \frac{1}{\mathcal{V}}\sum_{\alpha=\uparrow,\downarrow} g_\alpha \sum_{\mathbf{k},\mathbf{k}',\mathbf{q}} c^\dagger_{\mathbf{k}'+\mathbf{q}\alpha}c_{\mathbf{k}'\alpha}d^\dagger_{\mathbf{k}-\mathbf{q}}d_{\mathbf{k}}, \quad (2)$$

where $\epsilon_{\mathbf{k}} = \hbar^2\mathbf{k}^2/(2m)$; m is the atom's mass; μ is the chemical potential of the gas of $|\mathrm{B}\rangle$ atoms; $\mathcal{V}$ is the volume of the system; $c^\dagger_{\mathbf{k}\alpha}$ ($c_{\mathbf{k}\alpha}$) is the creation (annihilation) operator for an impurity particle in state $\alpha \in \{\uparrow, \downarrow\}$ with momentum $\hbar\mathbf{k}$; and $d^\dagger_{\mathbf{k}}$ and $d_{\mathbf{k}}$ are the creation and annihilation operators for a particle in the bath $|\mathrm{B}\rangle$ with momentum $\hbar\mathbf{k}$, respectively. The coupling constants g_α are connected to the s-wave scattering lengths $a_{\alpha\mathrm{B}}$ by the Lippmann–Schwinger equation in the infinite-volume limit (Supplementary Section I). In the single-impurity limit, we can neglect interactions between atoms in the states $|\uparrow\rangle$ and $|\downarrow\rangle$.

Extracting the zero crossing

The zero crossing is extracted without a priori knowledge of the functional form of M using a linear fit in the range $M \in [-0.3, 0.3]$ in the vicinity of $M = 0$. Additionally, the data are fitted with the $T > 0$ extension of model equation (1), using the bath temperature T ($\approx T_\mathrm{spin}$) as an input parameter. These two methods have been checked to be consistent. We perform at least three repetitions for each data point for the steady-state spectrum around the zero crossing.

Zero crossing from spectral functions

The magnetization can be calculated using the exact relation $N_\alpha = \int \mathrm{d}\omega(\sum_{\mathbf{q}} A_{\alpha\alpha}(\mathbf{q}, \omega))/(\mathrm{e}^{\beta(\hbar\omega - \mu_\mathrm{imp})} + 1)$ between the populations N_α (where $\alpha \in \{\uparrow, \downarrow\}$) and the equilibrium spectral functions $A_{\alpha\alpha}(\mathbf{q}, \omega)$ in the presence of the drive; μ_imp is the impurity chemical potential; and $\beta^{-1} = k_\mathrm{B}T$. In the single-impurity limit, $\mu_\mathrm{imp} \to -\infty$, and it thus drops out of the expression for M. The resulting expression is evaluated using the equilibrium spectral functions from the T-matrix approximation. In practice, we also calculate $M(\Delta)$ using the impurity free energy[27] as the numerical convergence of the integrals is improved. The zero crossing is then extracted as in the experiment, from a linear fit to $M(\Delta)$.

To get a qualitative understanding of the T-matrix results, we compare them with the zero crossings obtained using a generic quasiparticle ansatz for the spectral functions[22] (Supplementary Section I). In this case, we find that $M = \left(\left(\Delta - \frac{E_\mathrm{p}}{\hbar}\right)\tanh\left(\frac{\beta\Omega_\mathrm{R}}{2}\right) + \frac{Z-1}{Z+1}\Omega_\mathrm{R}\right)/\left(\Omega_\mathrm{R} + \frac{Z-1}{Z+1}\left(\Delta - \frac{E_\mathrm{p}}{\hbar}\right)\tanh\left(\frac{\beta\Omega_\mathrm{R}}{2}\right)\right)$, where $\Omega_\mathrm{R} \approx \sqrt{Z\Omega_0^2 + \left(\Delta - \frac{E_\mathrm{p}}{\hbar}\right)^2}$. This reduces to the $T > 0$ generalization of equation (1) with $Z = 1$. We obtain an analytical expression for the zero crossing in the weak- and strong-drive limits:

$$\hbar\Delta_0 = \begin{cases} E_\mathrm{p} - \frac{1}{2}\hbar\Omega_0(Z-1) & \hbar\Omega_0 \gg E_\mathrm{F} \\ E_\mathrm{p} + 2k_\mathrm{B}T\,\mathrm{arctanh}\left(\frac{1-Z}{Z+1}\right) & \hbar\Omega_0 \ll E_\mathrm{F}. \end{cases} \quad (3)$$

In particular, for $\hbar\Omega_0 \ll E_\mathrm{F}$, we find $\hbar\Delta_0 = E_\mathrm{p}$ at $T = 0$. However, away from this limit, the zero crossing is shifted away from the polaron energy.

Effect of non-zero $k_\mathrm{F}a_{\downarrow\mathrm{B}}$

In our T-matrix approximation, we take into account the effect of a non-zero $k_\mathrm{F}a_{\downarrow\mathrm{B}}$. In our experiment, $k_\mathrm{F}a_{\downarrow\mathrm{B}}$ is small and positive, leading to the existence of a repulsive polaron in the $|\downarrow\rangle$ state. The dominant effect on Δ_0 is a shift in the polaron energy by the ($|\downarrow\rangle$ state) repulsive polaron energy[18] (Supplementary Section I). The effect of non-zero $k_\mathrm{F}a_{\downarrow\mathrm{B}}$ on Γ and the renormalized Rabi frequency Ω_R (Fig. 3) is visible in the large $\hbar\Omega_0/E_\mathrm{F}$ limit in the difference between the black lines and the grey lines (where we set $k_\mathrm{F}a_{\downarrow\mathrm{B}} = 0.16$ and $k_\mathrm{F}a_{\downarrow\mathrm{B}} = 0$, respectively). Note that the finite-temperature effect can be neglected in the limit $\hbar\Omega_0/E_\mathrm{F} \gg 1$.

Data availability

Experimental data displayed in the figures of the main text are available via figshare at https://doi.org/10.6084/m9.figshare.25041986 (ref. 36). Source data are provided with this paper.

Code availability

The codes for the theoretical calculations are available from A.S. (aschu@umd.edu) upon request.

References

36. Vivanco, F. J. et al. The strongly driven Fermi polaron. *figshare* https://doi.org/10.6084/m9.figshare.25041986 (2024).

Acknowledgements

We thank E. Altman, F. Chevy, E. Crane, E. Demler, Z. Hadzibabic, P. Julienne, C. Kuhlenkamp, J. Levinsen, M. Parish and R. Schmidt for discussions. We thank F. Scazza and G. Roati for sharing their experimental data. We are particularly grateful to B. Mulkerin for sharing insights on the numerical evaluation of the magnetization. This work was supported by the NSF (grant numbers PHY-1945324 and PHY-2110303), DARPA (grant number W911NF2010090), the David and Lucile Packard Foundation, and the Alfred P. Sloan Foundation. G.L.S. acknowledges support from the NSF Graduate Research Fellowship Program. A.S. acknowledges support from the US Department of Energy (DOE), Office of Science, National Quantum Information Science Research Centers, Quantum Systems Accelerator, and the

US DOE Office of Science, Office of Advanced Scientific Computing Research (ASCR) Quantum Computing Application Teams program, under fieldwork proposal number ERKJ347. M.K. acknowledges support from the Deutsche Forschungsgemeinschaft (DFG, German Research Foundation) under Germany's Excellence Strategy–EXC–2111–390814868, DFG grant numbers KN1254/1-2, KN1254/2-1 and TRR 360-492547816, and from the European Research Council (ERC) under the European Union's Horizon 2020 research and innovation programme (grant agreement number 851161), as well as the Munich Quantum Valley, which is supported by the Bavarian state government with funds from the Hightech Agenda Bayern Plus.

Author contributions

F.J.V., A.S. and S.H. contributed equally to this work. F.J.V. and S.H. obtained and analysed the experimental data. A.S. performed the theoretical calculations. All authors contributed to the discussion of the results and the writing of the paper.

Competing interests

The authors declare no competing interests.

Additional information

Supplementary information The online version contains supplementary material available at https://doi.org/10.1038/s41567-025-02799-8.

Correspondence and requests for materials should be addressed to Alexander Schuckert or Songtao Huang.

Peer review information *Nature Physics* thanks Giulia Del Pace and the other, anonymous, reviewer(s) for their contribution to the peer review of this work.